Geothermics 83 (2020) 101731

Contents lists available at ScienceDirect

Geothermics

journal homepage: www.elsevier.com/locate/geothermics

Local earthquake tomography of the Larderello-Travale geothermal field

M. Bagagli[a,*], E. Kissling[a], D. Piccinini[b], G. Saccorotti[b]

[a] Institute of Geophysics, ETH-Zürich, Switzerland
[b] Istituto Nazionale di Geofisica e Vulcanologia – Sezione di Pisa, Italy

ARTICLE INFO

Keywords:
Local earthquake tomography
Geothermal field seismotectonics
New P-wave velocity model

ABSTRACT

The Larderello-Travale Geothermal Field in South-West Tuscany (Italy) is the oldest and among the most productive geothermal fields in the world. A new 3D model of seismic P-wave velocity (V_P) of the upper crust beneath the geothermal field is derived by inverting a set of highly consistent travel-times from local-earthquakes. Results document a marked correlation of V_P with previously described, high-reflectivity horizons. We also determined a low velocity body (V_P ~5 km s^{-1}) culminating at depths of about 7 km, with estimated volume of 35–40 km^3. Such low velocities are consistent with a granite at temperatures above 700 °C, thus in a partially-molten status.

1. Introduction

Located in central Tuscany, Italy, the Larderello-Travale Geothermal field (LTGF; Fig. 1) is the oldest and among the most productive geothermal systems of the world. With a gross electricity generation of more than 4800 GW h per year, the LTGF accounts for about 10% of the current global geothermal electric energy production, and it contributes for the 2% to the Italian electric power needs (Razzano and Cei, 2015).

The LTGF is a steam-dominated system. The average composition of the extracted steam is 95% H_2O and 5% CO_2. The fluid's origin is mainly meteoric with a minor contribution of thermo-metamorphic and magmatic provenience (D'Amore and Bolognesi, 1994; Manzella et al., 1998).

About 230 production wells are presently active at the LTGF, extracting steam at temperatures and pressures spanning the 150–270 °C and 0.2–2 MPs intervals, respectively. The productive horizons are located over the 500–4500 m depth range.

As a part of the strategies for the sustainable management of the reservoir, deep drilling is now playing a major role (Barelli et al., 2000). Current exploration programs also focuses on the seek for high-temperature reservoirs hosting fluids at super-critical conditions (Bertani et al., 2018). Since super-critical fluids have a heat capacity which is much higher than that of sub-critical ones, the former resources are particularly well-suited for energy production.

So far, most of the subsoil images at the LTGF have been derived from 2- and 3-D seismic reflection surveys (e.g., Casini et al., 2010 and references therein). Nonetheless, a few imaging efforts have also been conducted using passive seismological methods. These include travel-time inversion of earthquake data from hypocenters at either teleseismic (Foley et al., 1992) or local (Vanorio et al., 2004; De Matteis et al., 2008; Saccorotti et al., 2014) distances, and the inversion of teleseismic Receiver Functions (Agostinetti et al., 2017). While we show results from V_P analysis only, previous studies also retrieved images of seismic S-wave velocities (V_S) and the mutual relationships between the ratio (V_P/V_S) and product ($V_P \times V_S$) of those two parameters. Results from these previous studies are summarized as follows. (1) A main reflective horizon, termed K-horizon (KH) (see also Section 2) overlay a marked increase of V_P (Vanorio et al., 2004). (2) Low V_P/V_S values characterize the exploited hydrothermal reservoirs, as a likely consequence of steam-bearing formations. In contrast, sparse regions at shallow depths exhibit high V_P/V_S and low $V_P \times V_S$ values, probably in association with areas of fluid condensation or recharge (De Matteis et al., 2008). (3) $V_P \times V_S$ images have been interpreted as if the KH delineates a transition toward a zone with a relatively lower crack accumulation and/or porosity (De Matteis et al., 2008). (4) Results from travel-time inversions brought no direct evidences for the presence of over-pressurized fluids at the KH, as previously hypothesized from reflection seismic data. Nonetheless, at least for the central sector of the LTGF, the KH has been observed to coincide with an abrupt termination of the anisotropic behavior of granites. This observation has been interpreted in terms of the sudden change in compressibility of the fluid filling the fractures, a condition which is achieved upon traversing the supercritical conditions (Agostinetti et al., 2017). (5) Furthermore, a middle-crustal low velocity body (LVB) in the center of the geothermal area was inferred at about 10 km depth by a 15–18% V_P reduction from

* Corresponding author.
E-mail address: matteo.bagagli@erdw.ethz.ch (M. Bagagli).

https://doi.org/10.1016/j.geothermics.2019.101731
Received 31 May 2018; Received in revised form 2 September 2019; Accepted 9 September 2019

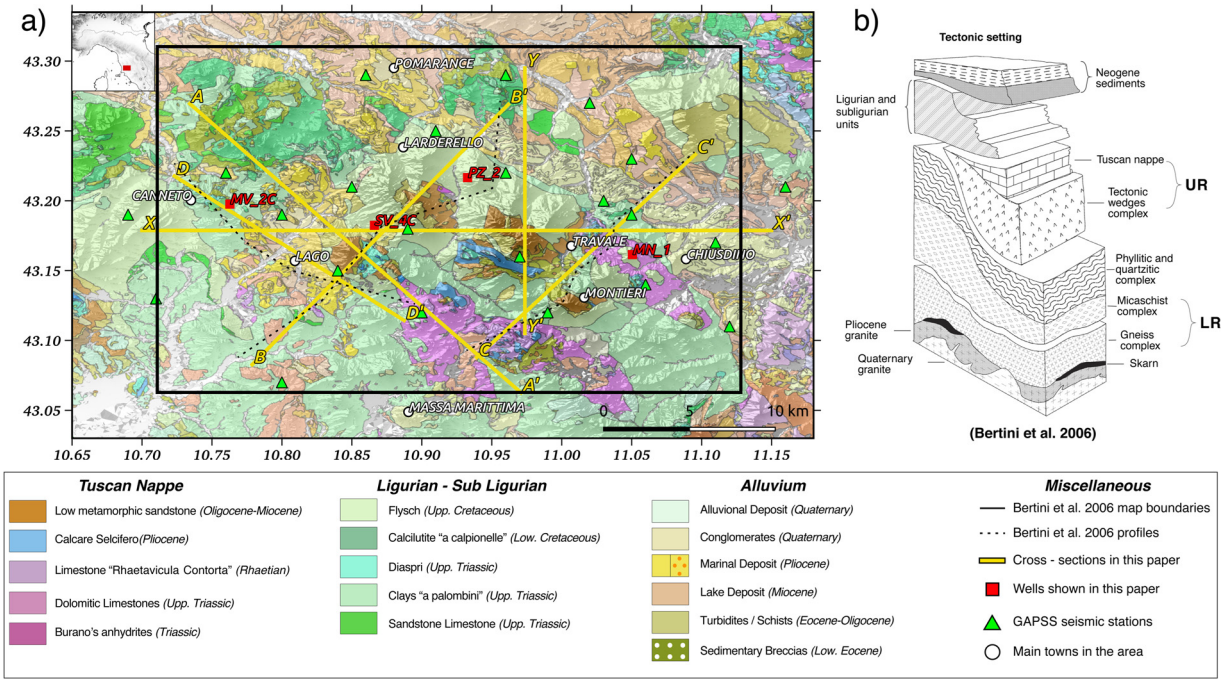

Fig. 1. (a) Map of the study region showing the main geological units in the area. The DEM used for this map and the other images contained in this paper is obtained from Tarquini et al. (2007, 2012) and the coordinates of the plotted profiles are reported in Table 1. (b) Schematic geological section redrawn from Bertini et al. (2006).

inversion of teleseismic travel-time residuals (Foley et al., 1992). The actual depth range of this LVB, however, remain unclear in the light of the long wavelength of teleseismic waves and consequent coarse resolution of the model.

Reliable information about the presence, location and volume of over-pressurized fluids (point 4 above) and the existence, location and geometry of the mid-crustal LVB (point 5 above) are of paramount relevance to better constrain the state and processes of the geothermal anomaly that feeds the near surface LTGF.

Local earthquake tomography (LET; Kissling, 1988) consists in the inversion of local earthquake's travel-times for solving the joint problem of hypocenter location and velocity model determination. It is now a widely-used tool for imaging both compressional- and shear-wave velocities in a variety of geodynamical settings. For the more specific case of active volcanic systems, earliest LET applications brought a significant contribution to the definition of shallow geological structures eventually identifying intrusive bodies, fluid pathways and accumulation areas (e.g., Jousset et al., 2011; Muksin et al., 2013; Zhang and Lin, 2014; Koulakov and Shapiro, 2014 and reference therein). These studies also showed that a comparison with independent data is needed to avoid misinterpretation of the geological structures, mitigating the intrinsic non-uniqueness of any geophysical inversion. A comprehensive review of tomographic studies in vulcanic areas is found in Koulakov and Shapiro (2014).

In recent years, LET methodologies have seen major improvements. These regard the implementation of sophisticated methods of wavefront tracking for solving the direct problem (i.e., ray-tracing), efficient inversion algorithms able to deal with very large datasets, and the proper consideration of finite-frequency wave propagation (see Rawlinson et al., 2014 for a review).

Nonetheless, the LET potentials are often hindered by the peculiarities of geothermal environments. First, illumination may be very irregular, as a consequence of the clustering of sources and limited number of stations. Second, due to the steep thermal gradient, hypocenters are usually shallow thus severely limiting the maximum resolvable depth. Finally, as for any other LET application, the quality of the input dataset is the most crucial aspect. This is tightly linked with the consistency in travel-time picking and associate uncertainties estimation.

Hence, the most crucial elements to improve LET for obtaining reliable images of the subsurface is the availability of a consistent set of arrival times, with a proper definition of uncertainties, and extensive use of synthetic tests for defining the correct parametrization of the model and assessing its resolution. All these topics are exhaustively addressed in the present work.

Following the above premises, in this work we conduct a P-wave veocity LET with the main goal of assessing the overall setting of the geothermal area, with particular reference to the most recent intrusive magmatic bodies. An additional objective concern the need of obtaining an improved velocity model for reliable earthquake location. This point assumes particular importance once addressing the increasingly-relevant issue of discriminating whether the recorded seismicity is natural, rather than induced by the geothermal exploitation processes. Finally, in complex geological settings such the LTGF, accurate P-wave images are required to enhance resolution and robustness in the migration of seismic reflection data.

2. Geological setting

From top to bottom, the tectono-stratigraphic sequence of the LTGF (Fig. 1b) consists of (1) post-orogenic sediments, of Mio-Pliocene to Quaternary age; (2) Flysch formations of the Ligurian units (Cretaceous-Eocene), with interspersed Ophiolitic blocks (late Jurassic); (3) Sandstones and Limestones formations from the Tuscan nappe (Late Triassic to early Miocene); (4) Evaporites and Phyllites of the tectonic wedge complex (Late Permian-Upper Triassic); (5) a Paleozoic metamorphic basement mainly composed by phyllites and gneiss. Post-orogenic sediments and Ligurian units act as the impermeable, cap-rock formation which contributes to the maintenance of the geothermal field (Fig. 1b).

The deep root of LTGF is represented by a plutonic complex constituted by the progressive stacking of different granitic magma bodies intruded between 3.8 and 1.3 Myr (Dini et al., 2005; Bertini et al., 2006; Casini et al., 2010). Cooling models for these earliest intrusions indicate that they cannot be responsible for the high temperatures of the fluids

Table 1
Coordinates of the discussed and plotted sections in the paper.

Profile	Start (lon–lat)	End (lon–lat)
AA'	10.7341–43.2695	10.9710–43.0625
BB'	10.7788–43.0827	10.9619–43.2690
CC'	10.9393–43.0879	11.0955–43.2331
DD'	10.7232–43.2177	10.8874–43.1143
XX'	10.7000–43.1787	11.1500–43.1787
YY'	10.9737–43.2950	10.9737–43.1050

presently exploited, rather suggesting the very recent emplacement of magma bodies at shallow depths (Spinelli et al., 2015). Until some 30 years ago, steam was extracted from an Upper Reservoir (UR) located at depths between 0.5 and 1.5 km within the Mesozoic limestones, anhydrites and dolomites of the Tuscan nappe (Fig. 1b). At present, the steam is mainly withdrawn from a Lower Reservoir (LR) located at depths of about 4 km (Bertini et al., 2006), and apparently in a static equilibrium with the overlying UR (Casini et al., 2010). The LR is associated with fracture zones within the metamorphic basement, and it hosts fluids with an average temperature of 300-350 °C and pressures of about 7 kPa.

Seismic reflection profiling identified two main horizons of high-amplitude, high-frequency reflections. The first one, is the aforementioned KH, while the second one is reported in the literature as H-horizon (HH hereinafter). KH is a regional feature which, below LTGF, is encountered over the 3–8 km depth range (Casini et al., 2010; Bertini et al., 2006). Occasionally the KH presents bright-spot features which suggest the presence of a fluid phase penetrating the rocks (Batini et al., 2003b).

The nature of the KH is still a matter of debate, and several geological interpretations have been proposed: (1) a kinematically-active rheological boundary separating a brittle upper part from a ductile lower part (Cameli et al., 1993); (2) a kinematic shear belt with entrapped fluids in fractured levels (Liotta and Ranalli, 1999) overlaying the brittle-to-ductile transition; (3) a thermo-metamorphic contact aureola at the top of the young (Quaternary) intrusions (Bertini et al., 2006).

The HH is more discontinuous and shallower (2–4 km) than the KH. It corresponds to productive layers of the LR, and it is interpreted as the top of pre-Quaternary granites; to this respect, the HH is interpreted as a "fossil" KH (Bertini et al., 2006).

LTGF is seismically active; for the last 20 years, the *Istituto Nazionale di Geofisica e Vulcanologia* (INGV) instrumental catalog (*cnt.rm.ingv.it*; last accessed January 25, 2019) reports seismicity rates of up to 30 earthquakes/month, with a maximum magnitude $M_L = 3.8$. Batini et al. (1985) observed a direct correlation between earthquakes occurrence and the rate of wastewater re-injection back in the subsurface. However, both the maximum magnitudes and the rate of earthquakes with $M > 2$ did not exhibit any correlation with the re-injection process. The same authors also noted that most of the epicenters were located in close proximity of active wells, an evidence which is also confirmed by our data (see Fig. 2). Following these arguments, Batini et al. (1985) argued that most of the seismicity at LTGF was induced by the re-injection activities. Nonetheless, historical records indicate that damaging earthquakes struck the LTGF well before geothermal exploitation started, with a maximum documented intensity of 7–8 on the Mercalli–Cancani–Sieberg scale associated with the 1724, $M = 5.4$ Travale earthquake (Rovida et al., 2016). As a consequence, discerning to which extent the current LTGF seismicity is related to the energy production cycle rather than to a natural background activity at the site is still a matter of debate.

3. Data

3.1. The experiment

The local earthquake dataset used for this study is obtained from the *Geothermal Area Passive Seismic Sources* (GAPSS) experiment carried out by the INGV between May 2012 and November 2013. During the experiment, up to 23 temporary seismic stations were operated within a 40 × 30 km area encompassing the whole LTGF, complementing the 2 permanent stations from INGV's national earthquake monitoring network (Fig. 1a). Throughout the duration of the survey, the overall deployment detected more than 2000 local earthquakes, with moment magnitudes spanning the $-0.3/+3.5 M_w$ range (Fig. S4b) (Saccorotti et al., 2014).

In order to get a high-quality and highly-consistent dataset, we adopted a semi-automated repicking procedure updated from that originally proposed by Di Stefano et al. (2006). The picking procedure is based on a successive application of two different auto-picking system: the Mannekeen Pix (Aldersons, 2004) and the **Ba***It* "Iterative Baer-Kradolfer picking" (Baer and Kradolfer, 1987). The latter, was developed ad-hoc to increase the recovery-ratio of P-phases picks and overcome the noise-generated artifacts that could mislead classical autopicking system. The tuning of this semi-automated procedure, required a manual repicking of a Reference Dataset (RD) consisting of 82 events for a total of ~1000 waveforms following the procedure described in Diehl et al. (2012). Both of these two automatic system were properly tuned using the above mentioned reference dataset. For a detailed description of the methodology and procedure the reader is referred to the Supplementary Information.

3.2. Inversion set-up and model parametrization

High-precision hypocenter locations throughout the area under investigation and a set of arrival time observations with consistent uncertainty information largely free of outliers are of crucial importance for the quality of LET inversion. Therefore, we applied the VELEST software (Kissling, 1988), to (1) calculate a minimum 1D velocity model (Min1D) (Fig. 2a) to be also used as initial reference model for the subsequent 3D tomographic inversion (Kissling et al., 1994), and (2) to filter the dataset for travel-time outliers on the basis of the joint hypocenter-velocity determination approach. Compared to the initial reference models used by previous studies, our Min1D model exhibits higher velocities than the model by Saccorotti et al. (2014), and stronger velocity gradient than the model by Vanorio et al. (2004) (Fig. 2a). However, our model and that from Vanorio et al. (2004) basically report the same velocities and gradients for the 1–4 km depth interval.

All the repicked events were then relocated using the Min1D model and corresponding station delays. From this catalogue, we selected 572 locations with azimuthal gap less than 180° and at least 6 P observations, thus obtaining a final data set of 4746 P-phase observations of quality class in the range 0–2 (Fig. 2c). Following the careful execution of the re-picking procedure (Fig. S1) the average observation uncertainty for this data set is on the order of ± 0.063 s.

For 3D tomographic inversion, we used the SIMULPS code (Thurber, 1984), and defined the initial reference model according to the aforementioned Min1D model (Fig. 2). For the 3D model parametrization, we tested three different arrangements with horizontal node spacing of 5 × 5 and 3 × 3 km, and layering intervals of 2 and 2.5 km (Fig. 2b). These different configurations were probed against their ability to recover amplitude and locations of synthetic velocity anomalies spanning the central part of the study area, where resolution is highest and rather uniform Kissling et al. (2001). Fig. 3 provides a summary of the results of these synthetic data tests obtained with different damping values. For each test parametrization, the best damping-values are marked with a green dashed box: for model 2 this value falls in between 1 and 2.5,

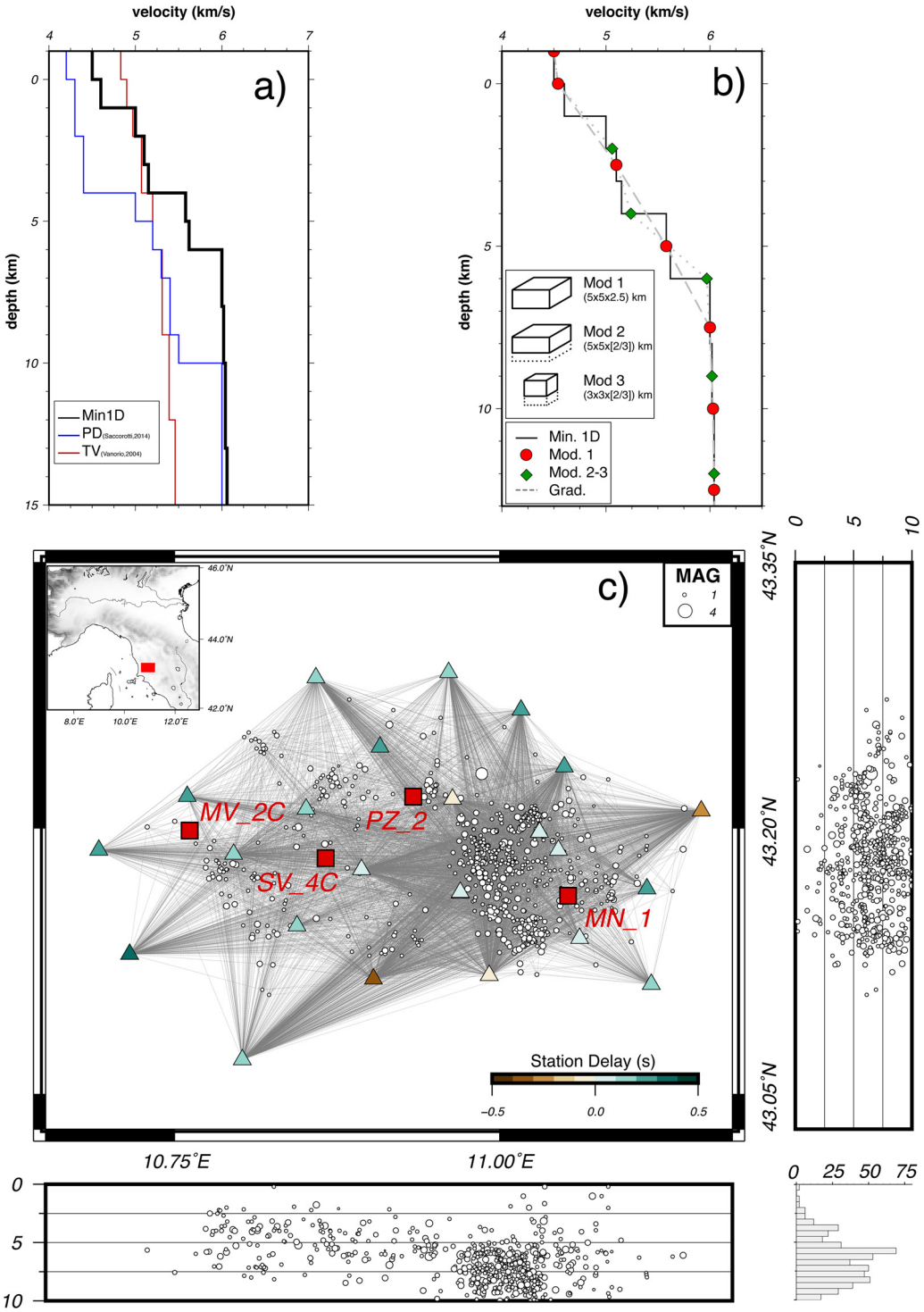

Fig. 2. Minimum 1D model for LTGF region. (a) 1D velocity profile resulting from this study, compared with those used in the literature (Saccorotti et al., 2014; Vanorio et al., 2004). (b) Re-parametrization of the Minimum 1D velocity model for the 3D grid used in subsequent inversion with SIMULPS. (c) Hypocenters distribution of relocated seismicity used for the 3D inversion: 572 well-locatable events with azimuthal gap less than 180° and P-observations number greater than 6 recorded during the GAPSS experiment. The main wells location referenced from Bertani et al. (2005) are plotted in (c) panel (red squares).

while for the two other models the optimal values are 2.5 (model 1) and 1 (model 3). Apart from defining the best damping values for the subsequent inversion of real data, these synthetics tests are also useful for gaining insights into possible artifacts resulting from velocity perturbations of the same sign being transferred to adjacent nodes along either the vertical (leakage) or horizontal (smearing) directions (Kissling et al., 2001). The final parametrization adopted for the 3D inversion is the one corresponding to Mod. 1 (5 × 5 × 2.5 km) with damping value of 2.5. As documented by the synthetic test results, this combination of parameters offers basically no smearing or leakage (as opposed to the other two solutions), perfect recovery of geometries and very good recovery of amplitudes within the well-resolved region as identified by the diagonal of the resolution matrix RDE (Fig. 3).

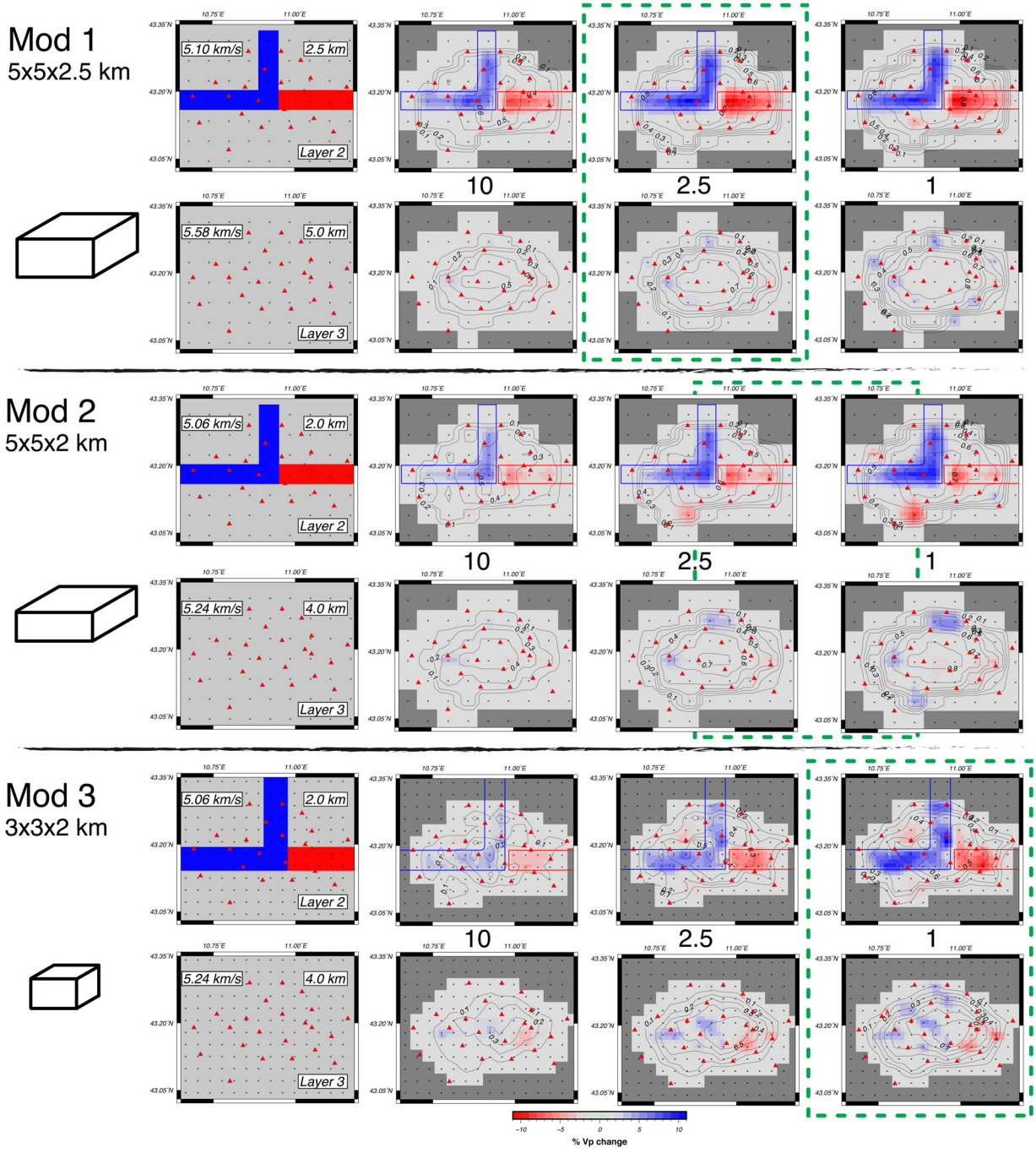

Fig. 3. Synthetic data resolution tests for the 3 different model parametrizations and damping parameters (10,2.5,1). For each model, dashed green boxes highlight the best value for the damping parameter. The black solid isolines represent the values of the diagonal element of the resolution matrix RDE. For each test, lateral velocity variations were introduced in Layer 2. Layer 3 without velocity anomaly is also shown to check for vertical leakage. We note that the geometry and the amplitude of the velocity anomalies are generally well-recovered within the area of RDE greater than 0.25 with damping 2.5 for model 1, with damping in the range of 2.5–1 for model 2 and with a damping value of 1 for model 3. Since vertical leakage and horizontal smearing is minimal for model 1, for the final 3D inversion we choose this model parametrization and a damping value of 2.5.

4. Results

The results of the 3D non-linear inversion are shown in Figs. 4–7. Within 4 iterations, the initial data variance of 0.025 s^2 (corresponding to a RMS-residual of 0.16 s^2) has been reduced by 80% to final data variance of 0.005 s^2 (RMS-residual of 0.07 s that compares well with the estimated average observation uncertainty of 0.063 s (Fig. 6c). The highly heterogeneous subsurface of LTGF is represented by lateral and vertical velocity variations spanning the 3.5–6.5 km s^{-1} range within the top 10 km of crust. The lowest velocities are those associated with the sedimentary basins mainly composed of Quaternary deposits in the southwestern and eastern parts of the study area (Fig. 1), as visible in the W–E section (XX') of Fig. 5a. The reported velocity values are significantly larger than the average interval velocity of 2.6–2.8 km s^{-1} reported by Batini and Nicolich (1985) and Bertini et al. (2005). Such discrepancy, however, may be explained in terms of (1) the low resolution of LET inversion for the shallowest layers, where the number of crossing rays is generally low, and (2) the reduced thickness of those post-orogenic, sedimentary formations once compared to the vertical layering of our discretized parameter space. The contacts between

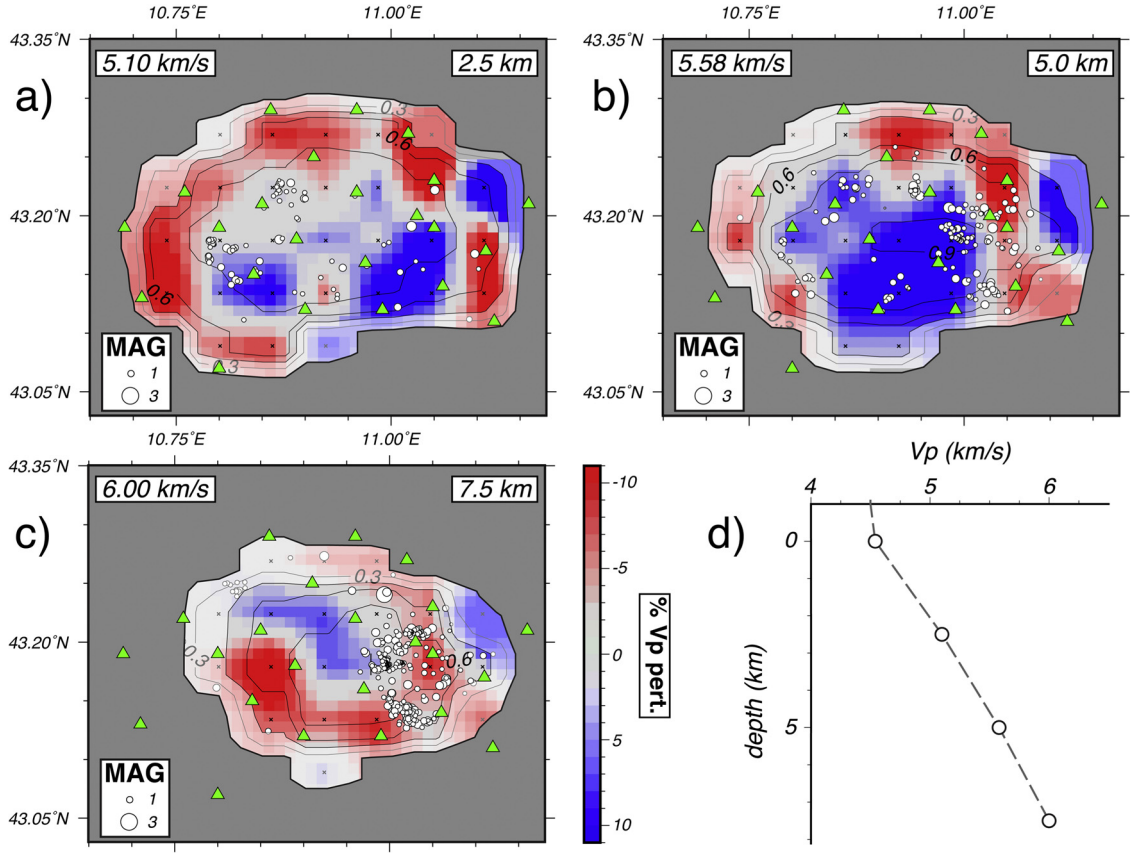

Fig. 4. Resulting tomographic images of the 3D subsurface velocity structure of LTGF. The different panels show horizontal-slices of velocity perturbations with respect to the initial model at 2.5 km (a), 5.0 km (b), 7.5 km (c) depths. (d) The initial 1D velocity model used for the inversion.

underlying Ligurian, Tuscan nappe, tectonic wedge and metamorphic complexes are not immediately discerned, even if several correspondences are found with the main features previously known from reflection seismology and drill-hole information (e.g., Bertini et al., 2006). The main findings of our study are summarized as follows:

Between 16 and 27 km into the profile of Fig. 5a, a dome-shaped high-velocity body (HVB) is detected. Bounded by a pronounced clustering of seismicity at its eastern side, the HVB is also clearly observed in the horizontal slices of Fig. 4 as a centered, positive perturbation with respect to the initial reference model. The upper topography of this body is closely followed by the KH. In its eastern portion (some 27 km into the W–E section (XX') of Fig. 5a) the HVB elongates upward, extending over the KH with velocities of up to 6 km s^{-1}.

A relevant low-velocity body (LVB) is imaged at the central-western sector of the geothermal field, with a minimum V_P on the order of 5 km s^{-1}) at depths of 7–8 km (see Figs. 5a–7). This depth range is still well-resolved by our inversion, and it is roughly consistent with the S-wave velocity minimum found by Agostinetti et al. (2017) from teleseismic receiver-function analysis (see Fig. 5d). However, the LVB appears to be significantly shallower than the low-velocity body imaged at 10 km depth by teleseismic tomography (Foley et al., 1992).

The pronounced HVB below the Travale area terminates abruptly moving eastward, and it is replaced by a deep-rooted, low-velocity body. Although not imaged in any of the previous LET studies (Vanorio et al., 2004; De Matteis et al., 2008; Saccorotti et al., 2014), the reliability of such negative anomaly is supported by our synthetic tests (Fig. 3).

For those locations where the HH has been documented directly by well-logging (Bertani et al., 2005; Casini et al., 2010), it correlates with velocities spanning the 5–5.4 km s^{-1} range. The same, general association is also found with those portions of the HH derived from interpolation of well data and seismic profiling illustrated by Bertini et al. (2006) and reported in our Fig. 6. The above velocity range is consistent with the compressional wavespeed of ≈5.4 km s^{-1} indicated by Bertini et al. (2005) for the metamorphic basement.

In agreement with the findings by Vanorio et al. (2004) the KH (grey lines in Fig. 5) generally marks the passage to a high-velocity substratum. This is particularly evident in the NW–SE section of Fig. 5d (yellow dashed line number 1), where the KH trace closely encompasses regions with velocities above 6 km s^{-1}.

While confirming some of the major structural features of the LTGF already shown by previous tomographic images, the above results also present new elements whose significance is discussed in the next section.

5. Discussion

A dome-shaped, high-velocity region spans the whole geothermal area over the 3–8 km depth range, being particular evident in correspondence of the HVB described at point 1 in the results section above. Coherently with the results by Vanorio et al. (2004) and De Matteis et al. (2008), the upper limits of the high-velocity regions are closely followed by the KH (Figs. 4–6). Although the nature of this reflective horizon is still under debate (see Section 2), two complementary evidences play against the hypothesis that it may correspond to the brittle-to-ductile transition, as previously postulated by Liotta and Ranalli (1999). The first, is that the KH topography has been found to be dissected by many discontinuities which, though not exhibiting any obvious correlation with surface tectonic lineaments, indicate tensional faulting in response to the regional, NE–SW distensive stress regime (Bertini et al., 2005). The second, is the presence of active seismogenic volumes beneath the KH (Figs. 5 and 6), which is again suggestive of a

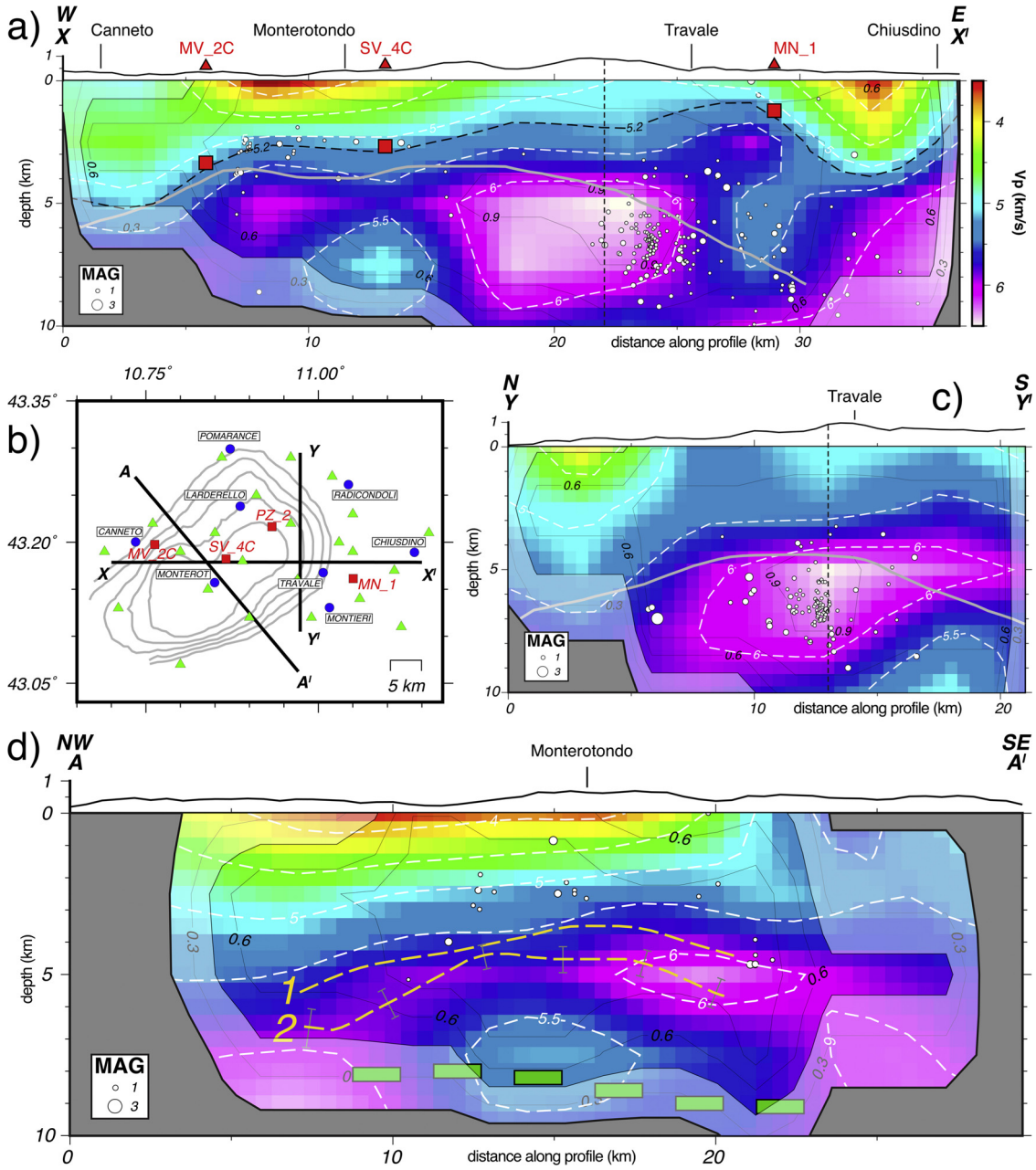

Fig. 5. Resulting tomographic images of the 3D subsurface velocity structure of LTGF. (a, c, d) Cross-sections displaying absolute seismic P-wave velocities. (b) Map displaying the locations of the profiles (black thick lines), the K-horizon isodepth from Barelli et al. (2000) (gray contour lines), the GAPSS array (green triangles), main towns (blue dots), and main wells location referenced from Bertani et al. (2005) (red squares). In (a) are plotted the HH's depths projected from well's log (red squares), the 5.2 km s^{-1} isoline (black dashed line), KH profile from Barelli et al. (2000) (gray line). (d) Cross-sections displaying absolute velocities along the profile by Agostinetti et al. (2017). KH from Barelli et al. (2000) (yellow dashed line 1), K-pulse from Agostinetti et al. (2017) (yellow dashed line 2), N-pulse receiver function profiling (thick green bar) from Agostinetti et al. (2017). In (a, c, d): the thin solid black isolines represent the values of diagonal resolution matrix (RDE); white dashed isolines represent the 0.5 km s^{-1} velocity isolines spanning the 4–6 km s^{-1} range; white circles represent the hypocenters within ± 2 km of the profile location. In (a–c) the black vertical dashed line corresponds to the intersection between the XX' and YY' profiles. The coordinates of the plotted profiles are reported in Table 1.

brittle behavior. Therefore, our favorite interpretation is that of the KH representing a contact aureole associated with thermo-metamorphic process at the top of the youngest (Quaternary) granitic intrusions, as postulated by Bertini et al. (2005, 2006).

Disregarding its nature, the inferred matching of the KH with the 450 °C isotherm (Cameli et al., 1998) indicates however that super-critical conditions may exist at and beneath that seismic marker. This has also been confirmed by the high-temperatures (T > 450–500 °C) encountered by both the San Pompeo 2 and DESCRAMBLE (Bertani et al., 2018) exploratory wells.

While Vanorio et al. (2004) interpreted the high-velocities underneath the KH in terms of either a strong lithology variation or a less fractured parts of the crystalline basement, the presence of seismogenic regions within the same depth range (see Fig. 5a and c) suggests local fracturing (and hence, high rock permeability), which could in turn constitute potential reservoirs of super-critical fluids. The same conclusions were reached by Agostinetti et al. (2017), who observed an abrupt termination of teleseismic P-wave anisotropy below the KH. The two apparently contrasting evidences of a still-fractured rock matrix and lack of anisotropy were interpreted by Agostinetti et al. (2017) in

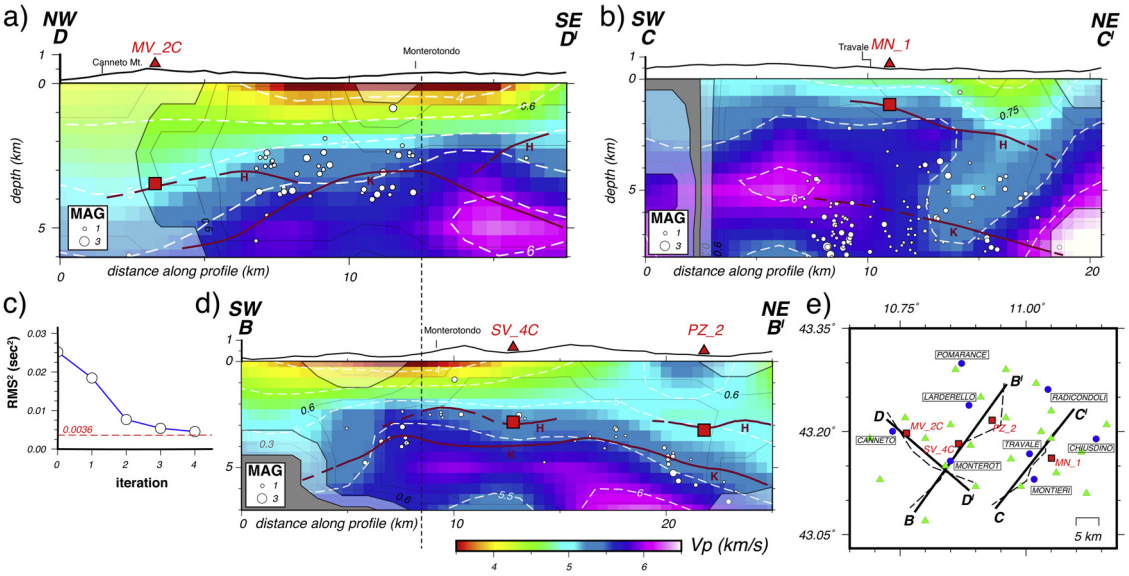

Fig. 6. Cross sections drawn for 3 profiles along with the seismic reflection results from Bertini et al. (2006). The H-horizon and K-horizon from Bertini et al. (2006) are shown by thick burgundry lines and the main wells H-horizon observation are marked by red-squares. (a) NW–SE (DD') section through Monterotondo. (b) SW–NE (CC') section through Travale. (c) Graphic showing the trend of RMS^2 after each iteration. The red dashed line represent the input error given by the observations quality class error's mean. The number of iteration stopped at 4 because the physical significance level of results was reached. (d) SW–NE (BB') section through Monterotondo. In (a, b, d): the thin solid black isolines represent the values of diagonal resolution matrix (RDE), white dashed isolines represent the 0.5 km s^{-1} velocity isolines ranging 4–6 km s^{-1}, white circles represent the hypocenters within ± 2 km of the profile location. (e) Reference map displaying the section's profiles (black thick lines) and with broken dashed lines the original profiles from Bertini et al. (2006), the GAPSS array (green triangles), main towns (blue dots), and main wells location referenced from Bertani et al. (2005) (red squares). The coordinates of the plotted profiles are reported in Table 1.

terms of a sudden change in compressibility of the fluids filling the fractures, a condition which is achieved upon reaching supercritical conditions. Most of the current LTGF production exploits fluids from the lower reservoir, which is generally associated with the HH. This particular horizon is interpreted in terms of a fractured thermo-metamorphic aureola at the top of the Pliocene granites, and it could represent the "fossil KH" (Bertini et al., 2006). Under this perspective, the marked upward elongation of the HVB at its eastern margin (point 1 above, Fig. 5a) can be interpreted as a protrusion of the Pliocenic intrusive bodies, consistently with the interpretation provided in pictorial view by Casini et al. (2010) for the same area. The close association of the HH occurrences with a narrow velocity interval (point 4 above) suggests that V_P images can be used for identifying the possible locations of such reflector at the scale of the whole geothermal area (Figs. 5 and 6).

Compressional wavespeed as low as ≈5 km s^{-1} reported for the LVB over the 7–8 km depth range (point 2 above; Figs. 5a–7) implies a significant decrease of both bulk and shear moduli, a condition which is consistent with the partial melting of the granitic rocks. For the pressures corresponding to depth interval of the LVB (around 200 MPs), the melting temperatures of granite are of at least 700 °C (Luth et al., 1964). We derive the size of the LVB by calculating the volume encompassed by the 5.5 km s^{-1} iso-surface, obtaining an estimate of about 35–40 km^3 (see Fig. 7). Given the impossibility to resolve depths greater than 9–10 km, this estimate probably represents a lower bound on the actual size of the VLB.

Finally, the deeply-rooted low-velocity anomaly located beneath the Travale area and described at point 3 above may be generally attributed to the NW–SE striking and N-dipping normal faults bordering the western side of the Radicondoli–Chiusdino graben (see Fig. 1), which might have caused a thickened uppermost crustal layer of lower velocities at the eastern margin of our profile. Additional, buried structures

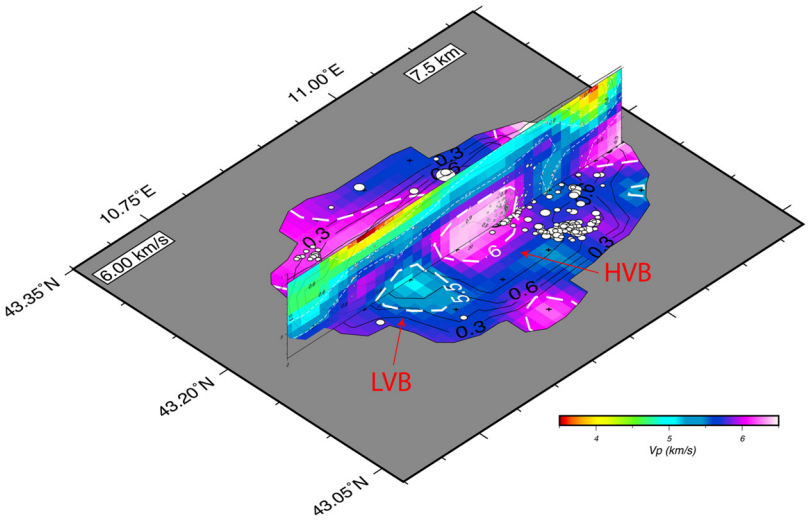

Fig. 7. 3D visualization of the final V_P velocity model obtained in this study. White dashed lines represent the velocity isolines. In thicker white-dashed line the 5.5 and 6 km s^{-1} isolines that bounds respectively the low- and high-velocity body (point 2 and 1 in Section 4). The volume of this low-velocity body, based on model-resolution, is estimated to be around 35–40 km^3.

recognized in the same area include (1) a set of normal faults dissecting the KH, likely responsible for the steep E-NE deepening of this latter horizon, and (2) a major, NS-striking, sub-vertical transcurrent fault with a dextral movement that horizontally displaces the above faults with Apenninic direction (see Figs. 8 and 10 in Fiordelisi et al. (2005). Taken all together, these tectonic features suggest the likely presence of a diffuse damage zone extending from the KH to the surface. This region could act as a preferential pathway for upward migration of fluids, which in turn would be responsible for the consistent thermal anomaly observed beneath the Travale area (e.g., Manzella et al., 2006; Sani et al., 2016).

6. Conclusion

In this work, we used local earthquakes data recorded by a dense, temporary deployment to derive a new image of P-wave velocities beneath the LTGF. P-wave arrival times have been repicked following a 3-step, semi-automated procedure, updated from a method previously proposed by Di Stefano et al. (2006). This procedure allowed to get a data set of highly-consistent arrival times with realistic error assessment. Furthermore, the resolution of the inversion procedure and reliability of the results were checked thoroughly using customized resolution tests (Fig. 3). In their general features, our velocity structure and hypocenters distribution confirm and complement the knowledge acquired through several previous studies about the internal structure of the LTGF (Vanorio et al., 2004; De Matteis et al., 2008; Bertini et al., 2006; Casini et al., 2010).

Due to the intrinsic limitations of the method, LET-derived images are not able to resolve velocity features at the scale of individual productive horizons. As a consequence, the results presented above do not have immediate implications for exploration purposes. Nonetheless, some of our findings contribute to a better understanding of the whole geothermal system, and to the identification of areas potentially hosting new productive reservoirs. To these purposes, we recognize the following elements.

(1) The detection of a LVB at the Western side of the geothermal area, most likely associated with the most recent and still cooling magmatic intrusion, whose depth appears to be significantly shallower than what previously hypothesized. The estimated temperature and size of this body (> 700 °C and 30 km^3, respectively) yield new constraints for any subsequent simulation effort aimed at predicting expected temperatures and flow rates for evaluating the geothermal potential of the area.

(2) The association of the (generally productive) HH horizon with a narrow velocity range could pave the way to the mapping of this particular reflective marker at the scale of the whole geothermal field. To this respect, however, it must be specified that neither the KH or HH are continuous throughout the LTGF. The 3D topographies of these markers reported thus far (e.g., Bellani et al., 2004; Bertini et al., 2006; Casini et al., 2010), derive in fact from extensive inter- and extrapolation in between and at the margins of the areas spanned by wells and seismic lines.

One of the still-pending questions regards the actual potential of the KH for hosting productive reservoirs. The high seismic impedance of this seismic marker, occasionally exhibiting bright-spot features, was interpreted as due to magmatic/metamorphic fluids, possibly in supercritical conditions. Evidence strengthening this interpretation was provided by the exploratory well San Pompeo 2, drilled on 1979 in the Lago area where the KH reaches its shallowest level. At a depth of about 2900 m, just above the KH, the drilling unexpectedly encountered high-temperature ($T > 400$ °C), high-pressure fluids which induced well blow-out and the eruption of a large amount of breccias and vein fragments (Bertani et al., 2018). In the same area, a second attempt of directly probing the KH has been conducted in 2017, within the frame of the *DESCRAMBLE* project. At the final depth of 2900 m, in the middle of the KH seismic reflections, the drilling encountered extremely high temperatures (507–517 °C), but no presence of fluids. As a consequence, the presence of exploitable fluids does not appear to be a persistent feature of the KH. Rather, that (occasional) presence could result from localized, small-scale weakness zones which guarantee hydraulic connectivity with the underlaying magmatic bodies. Approaching this issue would require integration of both V_P and V_S images with S-wave anisotropy data, at a resolution which is not achievable with the data presently available.

Declaration of Competing Interest

The authors declare that they have no known competing financial interests or personal relationships that could have appeared to influence the work reported in this paper.

Aknowledgment

Matteo Lupi and an anonymous reviewer are acknowledged for the constructive criticisms that greatly helped improving the quality of the manuscript. This work has been supported by the Swiss National Foundation grant CRS112_154434. Waveforms can be obtained upon request to Gilberto Saccorotti (gilberto.saccorotti@ingv.it) and Davide Piccinini (davide.piccinini@ingv.it) while travel-times picks and the model shown in the article can be obtained from the corresponding author.

Appendix A. Supplementary data

Supplementary data associated with this article can be found, in the online version, at https://doi.org/10.1016/j.geothermics.2019.101731.

References

Agostinetti, N.P., Licciardi, A., Piccinini, D., Mazzarini, F., Musumeci, G., Saccorotti, G., Chiarabba, C., 2017. Discovering geothermal supercritical fluids: a new frontier for seismic exploration. Sci. Rep. 7 (1), 14592.
Aldersons, F., 2004. Toward a Three-Dimensional Crustal Structure of the Dead Sea Region from Local Earthquake Tomography (Ph.D. thesis). Citeseer.
Baer, M., Kradolfer, U., 1987. An automatic phase picker for local and teleseismic events. Bull. Seismol. Soc. Am. 77 (4), 1437–1445.
Barelli, A., Bertini, G., Buonasorte, G., Cappetti, G., Fiordelisi, A., 2000. Recent deep exploration results at the margins of the Larderello-Travale geothermal system. Proceedings World Geothermal Congress 965–970.
Batini, F., Nicolich, R., 1985. P and S reflection seismic profiling and well logging in the Travale geothermal field. Geothermics 14 (5–6), 731–747.
Batini, F., Console, R., Luongo, G., 1985. Seismological study of Larderello-Travale geothermal area. Geothermics 14 (2–3), 255–272.
Batini, F., Brogi, A., Lazzarotto, A., Liotta, D., Pandeli, E., 2003b. Geological features of Larderello-Travale and Mt. Amiata geothermal areas (southern Tuscany, Italy). Episodes 26 (3), 239–244.
Bellani, S., Brogi, A., Lazzarotto, A., Liotta, D., Ranalli, G., 2004. Heat flow, deep temperatures and extensional structures in the Larderello geothermal field (Italy): constraints on geothermal fluid flow. J. Volcanol. Geothermal Res. 132 (1), 15–29.
Bertani, R., Bertini, G., Cappetti, G., Fiordelisi, A., Marocco, B.M., 2005. An update of the Larderello-Travale/Radicondoli deep geothermal system. Proceedings World Geothermal Congress 24–29.
Bertani, R., Büsing, H., Buske, S., Dini, A., Hjelstuen, M., Luchini, M., Manzella, A., Nybo, R., Rabbel, W., Serniotti, L., 2018. The first results of the Descramble project. Proceedings, 43rd Workshop on Geothermal Reservoir Engineering. Stanford University, Stanford, CA.
Bertini, G., Casini, M., Ciulli, B., Ciuffi, S., Fiordelisi, A., 2005. Data revision and upgrading of the structural model of the Travale geothermal field (Italy). Proceedings of the 2005 World Geothermal Congress 1–4.
Bertini, G., Casini, M., Gianelli, G., Pandeli, E., 2006. Geological structure of a long-living geothermal system, Larderello, Italy. Terra Nova 18 (3), 163–169.
Cameli, G., Dini, I., Liotta, D., 1993. Upper crustal structure of the Larderello geothermal field as a feature of post-collisional extensional tectonics (southern Tuscany, Italy). Tectonophysics 224 (4), 413–423.
Cameli, G., Dini, I., Liotta, D., 1998. Brittle/ductile boundary from seismic reflection lines of southern Tuscany (northern Apennines, Italy). Mem. Soc. Geol. It. 52, 153–162.
Casini, M., Ciuffi, S., Fiordelisi, A., Mazzotti, A., Stucchi, E., 2010. Results of a 3D seismic survey at the Travale (Italy) test site. Geothermics 39 (1), 4–12.
D'Amore, F., Bolognesi, L., 1994. Isotopic evidence for a magmatic contribution to fluids of the geothermal systems of Larderello, Italy, and the Geysers, California. Geothermics 23 (1), 21–32.

De Matteis, R., Vanorio, T., Zollo, A., Ciuffi, S., Fiordelisi, A., Spinelli, E., 2008. Three-dimensional tomography and rock properties of the Larderello-Travale geothermal area, Italy. Phys. Earth Planet. Inter. 168 (1), 37–48.
Di Stefano, R., Aldersons, F., Kissling, E., Baccheschi, P., Chiarabba, C., Giardini, D., 2006. Automatic seismic phase picking and consistent observation error assessment: application to the Italian seismicity. Geophys. J. Int. 165 (1), 121–134.
Diehl, T., Kissling, E., Bormann, P., 2012. Tutorial for consistent phase picking at local to regional distances. New Manual of Seismological Observatory Practice 2 (NMSOP-2) GeoForschungsZentrum pp. IS-11.
Dini, A., Gianelli, G., Puxeddu, M., Ruggieri, G., 2005. Origin and evolution of Pliocene–Pleistocene granites from the Larderello geothermal field (Tuscan Magmatic Province, Italy). Lithos 81 (1–4), 1–31.
Fiordelisi, A., Moffatt, J., Ogliani, F., Casini, M., Ciuffi, S., Romi, A., 2005. Revised processing and interpretation of reflection seismic data in the Travale geothermal area (Italy). Proceedings World Geothermal Congress 1–10.
Foley, J.E., Toksoz, M.N., Batini, F., 1992. Inversion of teleseismic travel time residuals for velocity structure in the Larderello geothermal field, Italy. Geophys. Res. Lett. 19 (1), 5–8.
Jousset, P., Haberland, C., Bauer, K., Arnason, K., 2011. Hengill geothermal volcanic complex (Iceland) characterized by integrated geophysical observations. Geothermics 40 (1), 1–24.
Kissling, E., 1988. Geotomography with local earthquake data. Rev. Geophys. 26 (4), 659–698.
Kissling, E., Ellsworth, W., Eberhart-Phillips, D., Kradolfer, U., 1994. Initial reference models in local earthquake tomography. J. Geophys. Res.: Solid Earth 99 (B10), 19635–19646.
Kissling, E., Husen, S., Haslinger, F., 2001. Model parametrization in seismic tomography: a choice of consequence for the solution quality. Phys. Earth Planet. Inter. 123 (2–4), 89–101.
Koulakov, I., Shapiro, N., 2014. Seismic tomography of volcanoes. Encycl. Earthqu. Eng. 1–18. https://doi.org/10.1007/978-3-642-36197-5_51-1.
Liotta, D., Ranalli, G., 1999. Correlation between seismic reflectivity and rheology in extended lithosphere: southern Tuscany, inner northern Apennines, Italy. Tectonophysics 315 (1–4), 109–122.
Luth, W.C., Jahns, R.H., Tuttle, O.F., 1964. The granite system at pressures of 4-10 kilobars. J. Geophys. Res. 69 (4), 759–773.
Manzella, A., Ruggieri, G., Gianelli, G., Puxeddu, M., 1998. Plutonic-geothermal systems of southern Tuscany: a review of the crustal models. Mem. Soc. Geol. It. 52, 283–294.
Manzella, A., Spichak, V., Pushkarev, P., Sileva, D., Oskooi, B., Ruggieri, G., Sizov, Y., 2006. Deep fluid circulation in the Travale geothermal area and its relation with tectonic structure investigated by a magnetotelluric survey. In: 31th Workshop on Geothermal Reservoir Engineering. Stanford University, Stanford, USA.
Muksin, U., Bauer, K., Haberland, C., 2013. Seismic Vp and Vp/Vs structure of the geothermal area around Tarutung (north Sumatra, Indonesia) derived from local earthquake tomography. J. Volcanol. Geothermal Res. 260, 27–42. https://doi.org/10.1016/j.jvolgeores.2013.04.012.
Rawlinson, N., Fichtner, A., Sambridge, M., Young, M.K., 2014. Seismic tomography and the assessment of uncertainty. In: In: Dmowska, R. (Ed.), Advances in Geophysics 55. Elsevier, pp. 1–76. https://doi.org/10.1016/bs.agph.2014.08.001. (Chapter 1).
Razzano, F., Cei, M., 2015. Geothermal power generation in Italy 2010–2014 update report. Proceedings World Geothermal Congress 2015, 19–24.
Rovida, A.N., Locati, M., CAMASSI, R.D., Lolli, B., Gasperini, P., 2016. Cpti15, The 2015 Version of the Parametric Catalogue of Italian Earthquakes.
Saccorotti, G., Piccinini, D., Zupo, M., Mazzarini, F., Chiarabba, C., Agostinetti, N.P., Licciardi, A., Bagagli, M., 2014. The deep structure of the Larderello-Travale geothermal field (Italy) from integrated, passive seismic investigations. Energy Proc. 59, 227–234.
Sani, F., Bonini, M., Montanari, D., Moratti, G., Corti, G., Del Ventisette, C., 2016. The structural evolution of the Radicondoli-Volterra basin (southern Tuscany, Italy): relationships with magmatism and geothermal implications. Geothermics 59, 38–55.
Spinelli, R., Casini, M., Costantino, N., Giudetti, G., Ciuffi, S., Dini, A., 2015. Anatomy of granite intrusions in the Travale geothermal field (Italy): a first geochemical-petrographic-spectral gamma ray log approach. In: Proceedings World Geothermal Congress. Melbourne. pp. 19–25.
Tarquini, S., Isola, I., Favalli, M., Mazzarini, F., Bisson, M., Pareschi, M.T., Boschi, E., 2007. Tinitaly/01: a new triangular irregular network of Italy. Ann. Geophys.
Tarquini, S., Vinci, S., Favalli, M., Doumaz, F., Fornaciai, A., Nannipieri, L., 2012. Release of a 10-m-resolution dem for the Italian territory: Comparison with global-coverage dems and anaglyph-mode exploration via the web. Comput. Geosci. 38 (1), 168–170.
Thurber, C., 1984. Simul3, Documentation of Earthquake Algorithms. pp. 15–17.
Vanorio, T., De Matteis, R., Zollo, A., Batini, F., Fiordelisi, A., Ciulli, B., 2004. The deep structure of the Larderello-Travale geothermal field from 3D microearthquake traveltime tomography. Geophys. Res. Lett. 31 (7).
Zhang, Q., Lin, G., 2014. Three-dimensional Vp and Vp/Vs models in the Coso geothermal area, California: seismic characterization of the magmatic system. J. Geophys. Res.-Solid Earth 119 (6), 4907–4922. https://doi.org/10.1002/2014JB010992.